

# Controllable Co-segregation Synthesis of Wafer-Scale Hexagonal Boron Nitride Thin Films

Chaoqua Zhang, Lei Fu, Shuli Zhao, Yu Zhou, Hailin Peng,\* and Zhongfan Liu\*

Hexagonal boron nitride (h-BN) is the representative 2D insulating material, possessing a large bandgap (6 eV),<sup>[1]</sup> excellent chemical and thermal stability, and a high thermal conductivity;<sup>[2]</sup> it has significant potential as a building block for high-quality integrated electronics and photonics.<sup>[3]</sup> Because insulating h-BN is isoelectronic and isostructural with semimetallic graphene — with a lattice mismatch of only 1.6% — while having distinct electronic properties,<sup>[2]</sup> atomic layers of h-BN are particularly suitable for integration with graphene, so as to enhance the performance of graphene electronics.<sup>[3c,4]</sup> Any practical applications of h-BN would require the development of low-cost, large-scale techniques for growing high-quality, large-area h-BN thin films, in which the film thickness can be controlled. Mechanical cleavage<sup>[3a]</sup> and liquid exfoliation<sup>[5]</sup> methods can provide micrometer atomic-layer-sized flakes of h-BN, but they are not suitable for large-area production. Current studies on the growth of large-area 2D h-BN films are focused on the normally used chemical vapor deposition (CVD) technique.<sup>[6]</sup> However, it is still a daunting task to achieve uniform h-BN thin films with controlled thickness because the CVD growth of h-BN on metal surfaces is greatly influenced by the exposure of gas precursors,<sup>[6e]</sup> crystal orientations,<sup>[6i,k]</sup> and grain boundaries.<sup>[6g]</sup> In addition to CVD methods, other methods, such as physical vapor deposition,<sup>[7]</sup> have been attempted to solve the issue of thickness control in h-BN growth. Here, we report a new approach for the synthesis of 2D h-BN thin films using the segregation phenomenon of boron and nitrogen. Using a rational design of growth substrates, sub-monolayer h-BN flakes, monolayer h-BN films, and multilayer h-BN thin films with controllable thickness were successfully prepared. Because solid-state precursors were used in the growth process, this method follows an underneath-growth model and exhibits good thickness- and location-control.

Segregation, which refers to the enrichment of solute constituents (such as C, B, and N atoms) onto the surface of metals, is a very common phenomenon in the heat treatment of metals. The well-known carbon segregation phenomenon

was discovered more than forty years ago,<sup>[8]</sup> and it has recently been proposed for the growth of high-quality graphene films.<sup>[9]</sup> The segregation phenomenon of B and N atoms was first discovered during the heat treatment of B- and N-doped stainless steels,<sup>[10]</sup> which has also been recently studied for h-BN growth.<sup>[11]</sup> For better control of the segregation process, we designed a sandwiched substrate with a solid-state (B,N)-layer between an Fe top layer and a Ni bottom layer, as illustrated in Figure 1a. The solid (B,N)-source was formed by electron-beam evaporation of commercial BN targets, and the corresponding chemical composition was determined to be  $B_{0.567}N_{0.063}C_{0.202}O_{0.168}$  based on the X-ray photoelectron spectroscopy (XPS) results (Figure S1, Supporting Information). Because Ni and Fe can react with B atoms producing  $Ni_xB$  ( $x = 1, 2, 3$ ) and  $Fe_xB$  ( $x = 1, 2$ ), respectively,<sup>[12]</sup> B atoms can dissolve in the bulk metals through reaction–diffusion with Ni and Fe. Along with the dissolution of B atoms into the metals, N species are brought into the metals in the form of a solid solution.<sup>[12]</sup> During the vacuum annealing of the Fe/(B,N)/Ni sandwiched substrate, dissolved N atoms and B atoms co-segregate from the bulk to the surface of the metals, producing the energetically stable form of h-BN layers (Figure 1a and Figure S2, Supporting Information).

Figure 1b shows typical XPS data of the h-BN film grown on the surface of the growth substrate. The B 1s and N 1s peaks are located at 190.4 and 397.9 eV, respectively, and they are similar to the reported values of CVD-grown h-BN films.<sup>[6g,h]</sup> The B:N atomic ratio calculated from the XPS data is 1.06:1, which is close to the 1:1 stoichiometry in h-BN. After transferring the films from the growth substrate to  $SiO_2/Si$  substrates using a poly(methyl methacrylate) (PMMA)-mediated transfer-printing technique (Figure S3, Supporting Information)),<sup>[13]</sup> we also detected obvious B 1s and N 1s peaks in the sample (Figure S4, Supporting Information), which indicate that only B–N bonds exist in the h-BN film. As shown in Figure 1c, the Raman spectrum of an approximately 8-nm-thick h-BN film transferred onto a  $SiO_2/Si$  substrate (with a 285-nm oxide layer) shows a dominant peak at  $1369\text{ cm}^{-1}$ , which is ascribed to the  $E_{2g}$  symmetry vibration mode of h-BN.<sup>[14]</sup> The photoluminescence background of h-BN is observed in this sample (Figure 1c) and other thinner samples including monolayer h-BN (Figure S5, Supporting Information), which can suppress relatively weak Raman signals. The photoluminescence backgrounds are also observed in CVD-grown h-BN samples,<sup>[6g,h,i]</sup> which may be ascribed to the impurity states from the grain boundaries of h-BN.<sup>[6d]</sup>

To further characterize the morphology and microstructure of h-BN, in addition to the 285-nm  $SiO_2/Si$  substrate, we transferred the h-BN thin film from the growth substrate to quartz substrates and transmission electron microscopy (TEM) grids.

Dr. C. H. Zhang, Prof. L. Fu, S. L. Zhao, Y. Zhou,  
Prof. H. L. Peng, Prof. Z. F. Liu  
Center for Nanochemistry  
Beijing National Laboratory for Molecular Sciences  
State Key Laboratory for Structural Chemistry of  
Unstable and Stable Species  
College of Chemistry and Molecular Engineering  
Academy for Advanced Interdisciplinary Studies  
Peking University  
Beijing, 100871, P. R. China  
E-mail: hlpeng@pku.edu.cn; zfliu@pku.edu.cn

DOI: 10.1002/adma.201304301



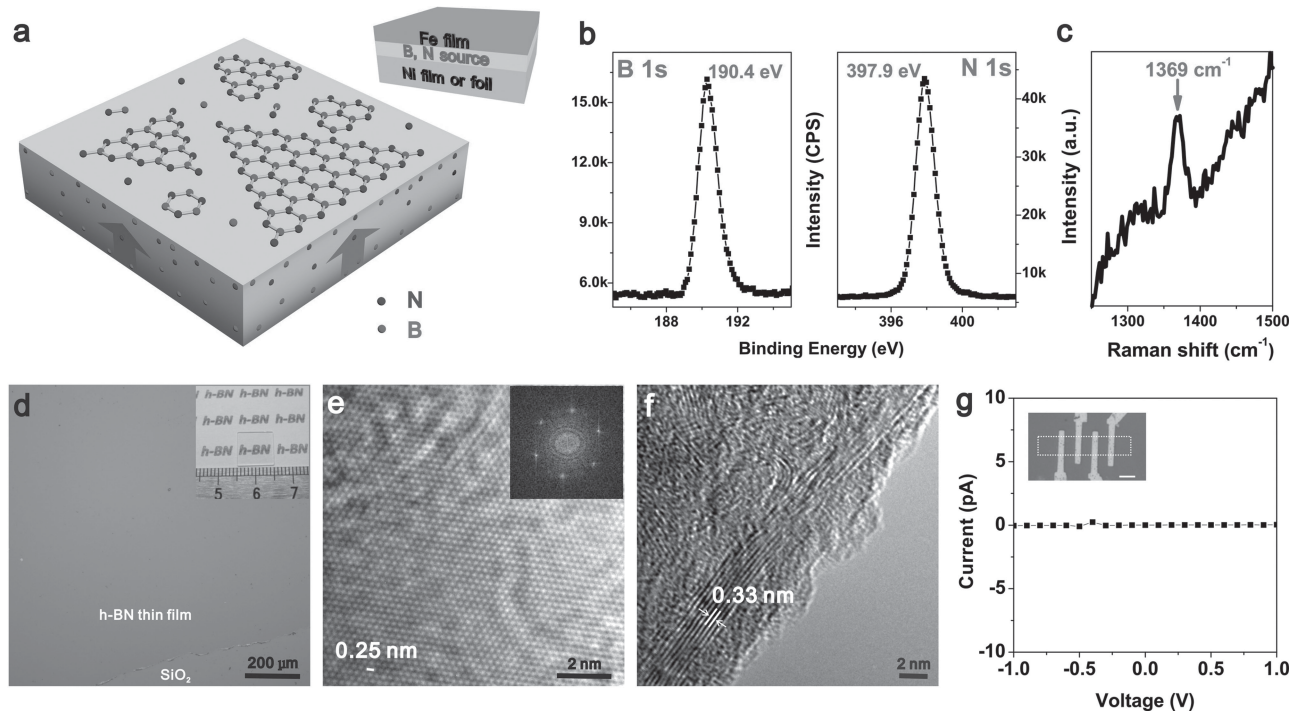


**Figure 1.** Schematic of the co-segregation method and characterization of h-BN thin films. a) Schematic of h-BN synthesis by the vacuum annealing of sandwiched substrates Fe/(B,N)/Ni. b) X-ray photoelectron spectra showing the B 1s and N 1s of h-BN on metals, revealing a B:N atomic ratio of 1.06:1. c) Raman spectrum of a h-BN film transferred onto a 285-nm SiO<sub>2</sub>/Si substrate, showing a peak at 1369 cm<sup>-1</sup>. d) Optical image of an h-BN film. The inset shows the h-BN film on a centimeter-sized quartz substrate with high transparency. e) High-resolution TEM image of a h-BN film, showing a fringe separation of 0.25 nm. The inset is the corresponding fast Fourier transform pattern, revealing the hexagonal structure of this material. f) High-resolution TEM image of a h-BN film edge, showing a 0.33 nm fringe separation. g) The current–voltage curve of a h-BN film shows excellent insulating nature. The inset is the optical image of the device configuration; the scale bar is 5 μm.

As shown in Figure 1d, the optical image exhibits a large-area, uniform, and continuous film of h-BN on the SiO<sub>2</sub>/Si substrate. On a quartz substrate, the h-BN thin film shows a high visible transparency (inset of Figure 1d). The high-resolution TEM image in Figure 1e displays the hexagonal lattice with a spacing of about 0.25 nm, consistent with the reported value for bulk h-BN.<sup>[2]</sup> The fast Fourier transform (FFT) pattern of Figure 1e displays only one set of hexagonal spots (inset of Figure 1e), confirming the single-crystalline nature of the examined area. Disorder-stacked multilayer h-BN is also found in other regions (Figure S6, Supporting Information). The high-resolution TEM image along the edge of a h-BN thin film in Figure 1f shows parallel line features with a separation of about 0.33 nm, which is in agreement with the interlayer distance of h-BN.<sup>[2]</sup> Selective-area electron diffraction (SAED) over a large area ( $\approx 1 \mu\text{m}^2$ ) shows multiple hexagonal spots (Figure S7, Supporting Information), which indicate that the h-BN film has multiple layers or domains in different orientations in the large region.

Carbon impurities can depress the insulating nature of h-BN and allowing current flow through the carbon-doped layers.<sup>[15]</sup> In our experimental design, the Fe film was used to suppress the occurrence of carbon impurities because carbon is highly soluble in Fe at high temperatures.<sup>[12]</sup> We specifically took electrical measurements of resistance to evaluate the quality of our h-BN thin films. The optical image in the inset of Figure 1g

shows the device configuration of h-BN that has been transferred onto the SiO<sub>2</sub>/Si substrate. As shown in Figure 1g, the current–voltage (*I*–*V*) curve shows no current flow through the devices in the scanned range of voltage. The measured current level of h-BN is below  $1 \times 10^{-12}$  A, indicating the excellent insulating nature of h-BN ( $> 10^6 \text{ M}\Omega$ ). Regardless of whether measurements were made using the two- or four-point probe technique, devices showed similar *I*–*V* characteristics.

Uniform and large-area monolayer h-BN thin films can be easily synthesized using this co-segregation method. As shown in Figure 2a, a 4 inch wafer-scale monolayer h-BN film is formed on the growth substrate after vacuum annealing (1 inch = 2.54 cm). Actually, the size and number of growth wafers are only restricted by the size of the vacuum furnace, showing that our method has potential for the mass production of h-BN thin films at low cost. As demonstrated in Figure 2b, monolayer h-BN films from different locations of the growth wafer are transferred successfully onto SiO<sub>2</sub>/Si substrates possessing 90 nm oxide layers; the films show uniform optical contrast as with the bare substrates. The corresponding scanning electron microscopy (SEM) image was conducted to identify the films from the substrates (Figure S8, Supporting Information), showing continuous and uniform films over large areas. Figure 2c shows the atomic force microscopy (AFM) image of an edge of a monolayer h-BN, and it confirms that the typical thickness is about 0.6 nm, which is consistent with the reported

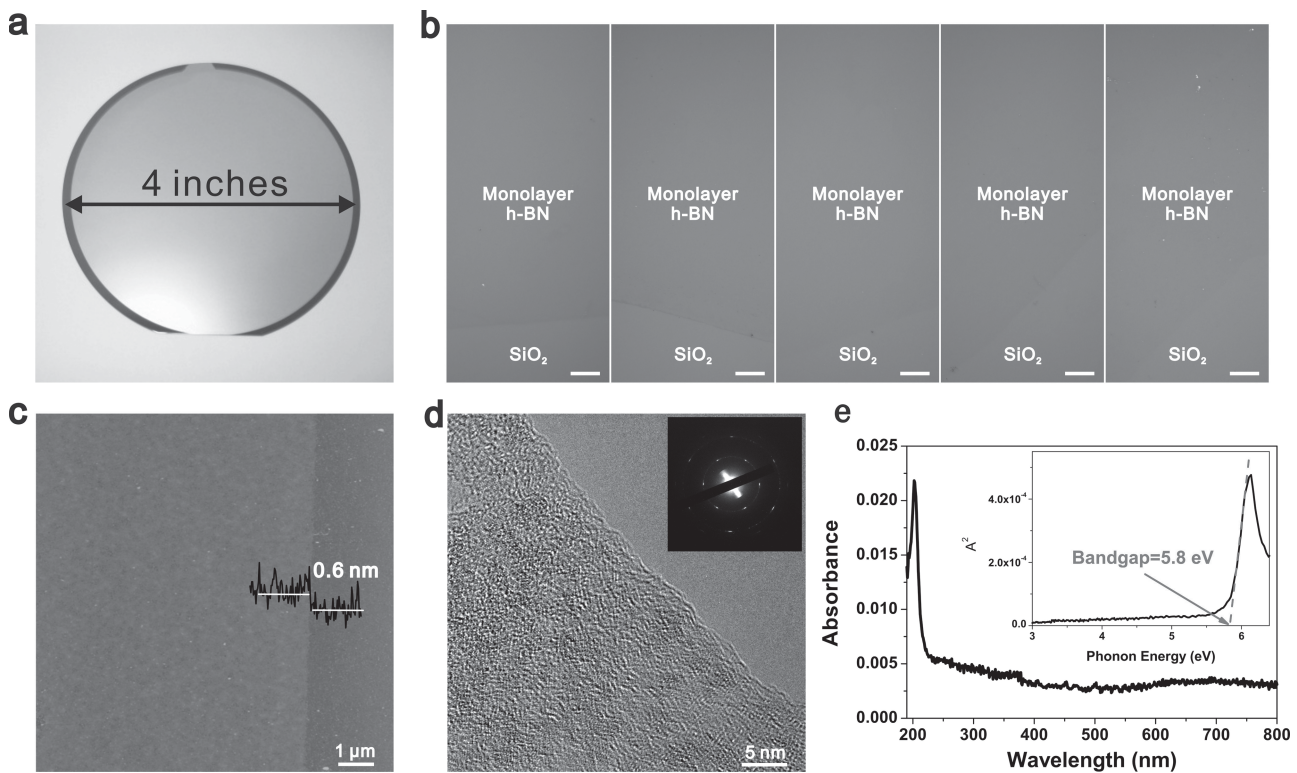


**Figure 2.** Characterization of the wafer-scale monolayer h-BN films. a) Photograph of a monolayer h-BN film grown on a 4-inch growth substrate b) Optical images of monolayer h-BN transferred onto 90-nm SiO<sub>2</sub>/Si substrates, showing different locations of the 4-inch wafer shown in (a). Scale bars are 20  $\mu\text{m}$ . c) Typical AFM image of a monolayer h-BN film. The inset indicates the AFM line profile across the edge of the film with a step of ca. 0.6 nm. d) High-resolution TEM image of a monolayer sample of h-BN near its edge. The inset is the SAED pattern, indicating that the monolayer h-BN is highly crystalline. e) Optical absorption spectrum of a monolayer h-BN film. The inset shows that the optical bandgap of monolayer h-BN is about 5.8 eV.

value for mechanically cleaved monolayer h-BN.<sup>[16]</sup> The adsorbed water or contamination layer might be responsible for the extra thickness in comparison with the actual thickness of monolayer h-BN ( $\approx 0.33$  nm).<sup>[16]</sup> Figure 2d shows the high-resolution TEM image of the edge of a monolayer h-BN film; the SAED patterns over small ( $\approx 0.16 \mu\text{m}^2$ ; inset) and large ( $\approx 1 \mu\text{m}^2$ ; Figure S9, Supporting Information) areas show single and multiple hexagonal diffraction patterns, respectively.

The light absorption of 2D materials has received much attention due to studies aimed at a basic understanding of their electron–phonon interactions.<sup>[17]</sup> As shown in Figure 2e, the monolayer h-BN film displays an absorbance peak at ca. 202 nm with an intensity of about 2.2%, which is close to the reported absorbance of graphene,  $A \approx \pi\alpha_R$  ( $\approx 2.3\%$ ),<sup>[18]</sup> where  $\alpha_R$  is the fine-structure constant. This experimental value is also consistent with a previous theoretical calculation, 2.1% (Equation S1, Supporting Information).<sup>[19]</sup> Considering the thickness of monolayer h-BN is 0.33 nm, the optical absorption coefficient ( $\alpha$ ) of h-BN is about  $0.066 \text{ nm}^{-1}$ . As shown in the inset of Figure 2e, the bandgap of our h-BN is also estimated by the plot of  $A^2$  vs. photon energy ( $\hbar\omega$ ),<sup>[20]</sup> which is  $\approx 5.8$  eV, close to the bandgap of h-BN crystal.<sup>[1b]</sup>

By controlling the thickness of the Fe film and (B,N)-source in the sandwiched substrates Fe/(B,N)-source/Ni, the thickness of the h-BN films can be controlled. The thickness of h-BN

thin films decreases linearly as the thickness of the Fe film increases, which can be seen from the optical contrast of the optical microscopy (OM) images in Figure 3a–c and the summarized function in Figure 3d. The thickness of h-BN films are determined by the corresponding optical absorption spectra (Figure S10, Supporting Information) using the linear relationship  $A = \alpha d$ , where  $\alpha$  is the optical absorption coefficient and  $d$  is the thickness. The relationship shown in Figure 3d can be understood by the reaction–diffusion process of Fe and B (Figure S2, Supporting Information). At the very beginning, the foremost N atoms diffused to the surface are desorbed since B atoms are not present at the surface. Thus the residual N atoms for h-BN growth decreases as the Fe film thickness increases. Adjusting the thickness of the (B,N)-source is another efficient way to control the thickness of the h-BN thin films. By designing sandwiched substrates with a patterned (B,N)-source (inset of Figure 3e), patterned h-BN thin films can be prepared (main image of Figure 3e), where the high-contrast square regions correspond to the growth substrates with a thicker patterned (B,N)-source. The relationship of the characteristics of the h-BN film and (B,N)-source is also systematically studied, as shown in the optical absorption spectra (Figure 3f) and the optical images (Figure S11, Supporting Information); the thickness of h-BN film increases as the thickness of the (B,N)-source increases (Figure 3g).

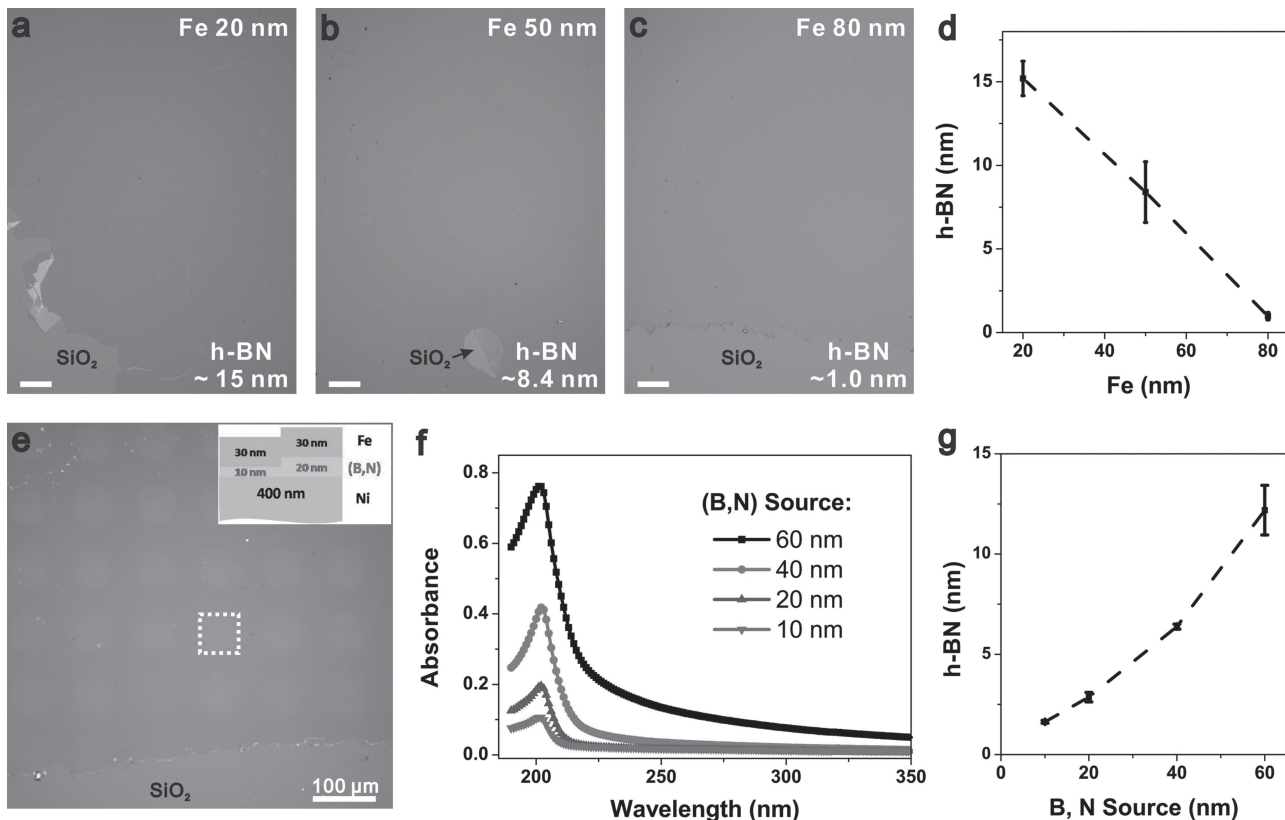


**Figure 3.** Thickness-control of h-BN thin films. a–c) Optical images of as-grown h-BN thin films grown using Fe films of different thicknesses. Scale bars are 100  $\mu\text{m}$ . d) Thickness of h-BN thin films as a function of Fe thickness. e) Optical image of patterned h-BN after vacuum annealing the sample at 1000 °C for 30 min. The inset shows a schematic of the substrate with a patterned (B,N)-source. Area within the dashed line corresponds to the regions with the 20-nm-thick (B,N)-source. f) Optical absorption spectra of h-BN films formed from (B,N)-sources of varying thickness. g) Thickness of h-BN thin film as a function of the thickness of the (B,N)-source.

Studies of the co-segregation growth mechanism of h-BN are relevant for the synthesis of high-quality h-BN thin films. To this end, we also systematically studied the initial nucleation state of the monolayer h-BN flakes on the Ni foils (Figure 4a,b) and Ni films (Figure 4d) substrates. Most of the sub-monolayer h-BN flakes grown on Ni foils exhibit triangular or truncated triangular shapes (Figure 4a,b); however some strip-like h-BN islands are also observed on other metal grains with different orientations (Figure S12, Supporting Information). As reported and discussed in previous studies,<sup>[6b,d,e,10c]</sup> the triangular shape, characteristic of sub-monolayer h-BN flakes grown on metals, is ascribed to the N-terminated edge of h-BN flakes (Figure 4c), which is the most energetically stable configuration. As illustrated in Figure 4c, N atoms prefer to sit on top of the metal atoms while B atoms can occupy hexagonal close packing (*hcp*) or face-centered cubic (*fcc*) hollow sites, leading to two kinds of h-BN domains with the N-terminated edge.<sup>[6d]</sup> For sub-monolayer islands grown on Ni films, however, only sporadic triangular h-BN flakes are observed (inset of Figure 4d). The dominant shapes of sub-monolayer h-BN flakes are consistent with the morphology of the step edges of the growth substrates (Figure 4d and Figure S13, Supporting Information), indicating the dominant step-flow growth mode on Ni film.<sup>[6d]</sup>

By increasing the supply of the (B,N)-source, fully covered monolayer and multilayer h-BN films are synthesized. As shown in Figure 4e, monolayer h-BN is quite uniform except for some sporadic multiple h-BN layers (inset of Figure 4e). For multilayer h-BN films, multilayer sites increase in both size and density. Thus the possible growth mechanism for the co-segregation of h-BN may be the layer-by-layer growth model for monolayer h-BN and the island-on-layer growth model for multilayer h-BN, which is similar to the CVD growth of h-BN.<sup>[6e]</sup> This growth mechanism may be explained by changes in the atom–surface interactions<sup>[6e]</sup> or the suppression of surface diffusion when monolayer h-BN fully covers the surface. Generally speaking, higher growth temperature helps increase the diffusion rate and improves the crystallinity of h-BN, which is revealed by the XPS data of the h-BN films grown at different temperatures (Figure S14, Supporting Information). So far, strictly uniform multilayer films of h-BN or graphene over a large area remain a challenge; they require improved synthesis design, where the growth substrates, precursors, and the mode of mass transport are optimized.

In summary, we developed a co-segregation method for growing wafer-scale, high-quality h-BN thin films with excellent insulating behavior. By vacuum annealing the sandwiched Fe/(B,N)/Ni growth substrates, B and N atoms are found to dissolve in the bulk of metals and then co-segregate onto the

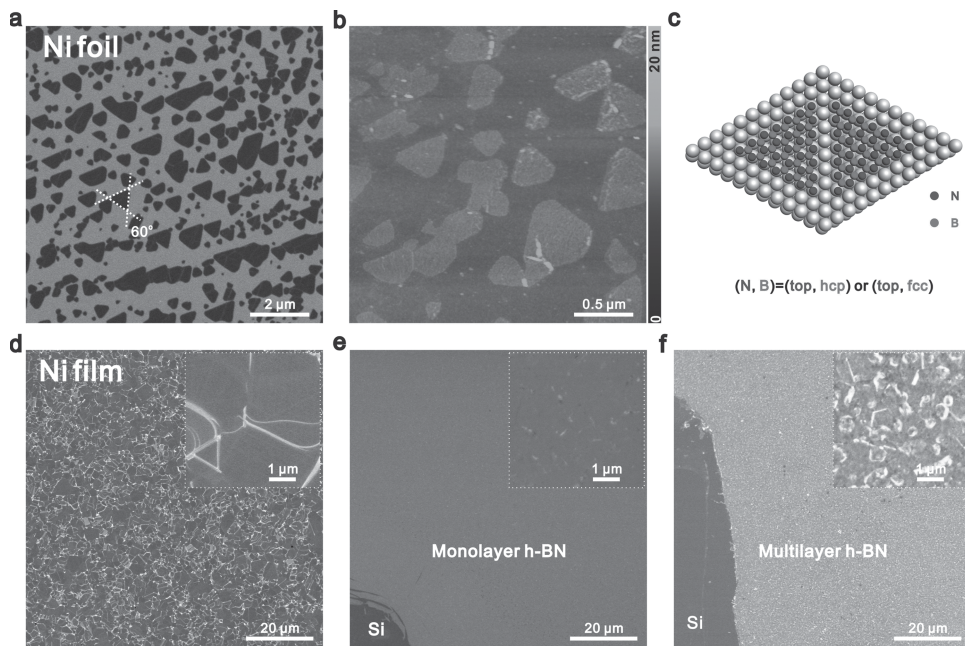


**Figure 4.** Morphology of sub-monolayer h-BN flakes and the study of the growth mechanism. a) SEM image of sub-monolayer h-BN flakes grown on a Ni foil substrate. b) AFM image of the sub-monolayer h-BN flakes transferred onto a  $\text{SiO}_2/\text{Si}$  substrate. c) Schematic illustration of the triangular sub-monolayer h-BN flakes on the  $\text{Ni}(111)$  surface with the N-terminated edge in two possible configurations. d) SEM image of sub-monolayer h-BN flakes grown on a Ni film substrate. e,f) SEM images of monolayer (e) and multilayer (f) h-BN thin films transferred onto Si substrates. The insets of (d–f) show the corresponding higher magnification SEM images.

surface of the growth substrates with the formation of h-BN thin films. Unlike when gas precursors are used in the traditional CVD method, solid precursors are used in this method, which follows an underneath-growth mode and allows thickness- and location-control. Sub-monolayer h-BN flakes, monolayer h-BN films, and multilayer h-BN thin films with different thickness are successfully prepared. Patterned h-BN thin films are achieved by pre-patterning the solid (B,N)-source. In addition, we examined the optical absorbance of monolayer h-BN, which is consistent with theoretical predictions. This co-segregation approach opens up a new pathway for large-batch production of h-BN thin films and may also be extended to the synthesis of other 2D materials and artificial hybrid materials.<sup>[21]</sup>

## Experimental Section

**Preparation of Growth Substrates Fe/(B,N)/Ni:** The Ni film (300–600 nm), (B,N)-source (5–60 nm), and Fe film (10–100 nm) were sequentially deposited onto  $\text{SiO}_2/\text{Si}$  substrates (with 300-nm oxide layer) from Ni, BN, and Fe targets using an electron beam evaporator (ULS400, Balzers, pressure  $1 \times 10^{-5}$  Pa before evaporation), which has four copper crucibles for different sources. The BN sources were produced by hot-pressed sintering h-BN powders. The weight purities of the commercial Ni, BN, and Fe sources were 99.99%, 99.99%, and 99.95%, respectively. The working pressure for Ni and Fe evaporation is  $1\text{--}3 \times 10^{-5}$  Pa, while the working pressure for the (B,N)-source is  $10^{-2}\text{--}10^{-1}$  Pa because of the decomposition of BN in the evaporation process. For the Ni foil (25  $\mu\text{m}$  thick, purity > 99.9%) growth substrates, the (B,N)-source and Fe film were directly deposited onto the Ni foils. The boron source can also serve as the (B,N)-source when deposition occurs under a  $\text{N}_2$  atmosphere (Figure S15, Supporting Information).<sup>[22]</sup>

**Growth Procedure:** The sandwiched  $\text{Fe}/(\text{B},\text{N})/\text{Ni}$  samples were loaded into the vacuum annealing furnace (VTHK-350, Beijing Technol Science Co., Ltd.) for annealing. After the furnace was evacuated to ca.  $5 \times 10^{-5}$  Pa, the samples were heated to desired temperatures (900–1100 °C) at a rate of 20 °C/min and maintained at the desired temperatures for 1–30 min with a working pressure of  $10^{-3}\text{--}10^{-4}$  Pa. Then the samples were allowed to cool to room temperature at a rate of 2–50 °C/min after the annealing power was shut off. The h-BN films could be detached from the growth substrates and transferred to target substrates using a PMMA-mediated transfer-printing technique (Figure S3, Supporting Information).<sup>[13]</sup>

**Samples Preparation:** The multilayer h-BN samples in Figure 1 were synthesized by vacuum annealing sandwiched substrates (Fe 50 nm/(B,N) 60 nm/Ni 500 nm) at 1100 °C for 10 min. The growth conditions of monolayer h-BN films in Figure 2 were Fe 30 nm/(B,N) 10 nm/Ni 400 nm at 1050 °C for 10 min. Figure 3a–d and f–g were obtained with the following conditions: Fe 20, 50, 80 nm/(B,N) 60 nm/Ni 400 nm at 1100 °C for 10 min, and Fe 30 nm/(B,N) 10, 20, 40, 60 nm/Ni 25  $\mu\text{m}$  at 1050 °C for 10 min, respectively. The vacuum annealing in Figure 4 was taken at 1100 °C for 1 min, and the corresponding  $\text{Fe}/(\text{B},\text{N})/\text{Ni}$  substrates were 15 nm/5 nm/25  $\mu\text{m}$  for Figure 4a,b; 15 nm/5 nm/400 nm for Figure 4d; 10 nm/6 nm/Ni 400 nm for Figure 4e; and 10 nm/12 nm/Ni 400 nm for Figure 4f.

**Characterization:** We characterized our samples using XPS (AXIS-Ultra), Raman spectroscopy (Horiba HR800, 457.9 nm, 2 mW), optical microscopy (Olympus BX51), SEM (Hitachi S-4800, 1 kV), AFM (Veeco Nanoscope IIIa, tapping mode), TEM (JEM 2100F, 200 kV), optical absorption spectroscopy (Lambda 950), and electrical measurements (Keithley, SCS-4200).

## Supporting Information

Supporting Information is available from the Wiley Online Library or from the author.

## Acknowledgements

We acknowledge financial support from the National Natural Science Foundation of China (nos. 51121091, 51072004, 21173004, 21222303, 51290272) and the National Basic Research Program of China (nos. 2011CB921904, 2011CB933003, 2013CB932603, and 2012CB933404).

Received: August 27, 2013

Revised: October 13, 2013

Published online: December 5, 2013

- [1] a) K. Watanabe, T. Taniguchi, H. Kanda, *Nat. Mater.* **2004**, *3*, 404; b) Y. Kubota, K. Watanabe, O. Tsuda, T. Taniguchi, *Science* **2007**, *317*, 932.
- [2] C. Oshima, A. Nagashima, *J. Phys.-Condens. Mater.* **1997**, *9*, 1.
- [3] a) K. S. Novoselov, D. Jiang, F. Schedin, T. J. Booth, V. V. Khotkevich, S. V. Morozov, A. K. Geim, *Proc. Natl. Acad. Sci. USA* **2005**, *102*, 10451; b) M. Xu, T. Liang, M. Shi, H. Chen, *Chem. Rev.* **2013**, *113*, 3766; c) L. Britnell, R. V. Gorbachev, R. Jalil, B. D. Belle, F. Schedin, A. Mishchenko, T. Georgiou, M. I. Katsnelson, L. Eaves, S. V. Morozov, N. M. Peres, J. Leist, A. K. Geim, K. S. Novoselov, L. A. Ponomarenko, *Science* **2012**, *335*, 947; d) L. Britnell, R. V. Gorbachev, R. Jalil, B. D. Belle, F. Schedin, M. I. Katsnelson, L. Eaves, S. V. Morozov, A. S. Mayorov, N. M. Peres, A. H. Neto, J. Leist, A. K. Geim, L. A. Ponomarenko, K. S. Novoselov, *Nano Lett.* **2012**, *12*, 1707.
- [4] a) C. R. Dean, A. F. Young, I. Meric, C. Lee, L. Wang, S. Sorgenfrei, K. Watanabe, T. Taniguchi, P. Kim, K. L. Shepard, J. Hone, *Nat. Nanotechnol.* **2010**, *5*, 722; b) R. Quhe, J. Zheng, G. Luo, Q. Liu, R. Qin, J. Zhou, D. Yu, S. Nagase, W. N. Mei, Z. Gao, J. Lu, *NPG Asia Mater.* **2012**, *4*, e6.
- [5] J. N. Coleman, M. Lotya, A. O'Neill, S. D. Bergin, P. J. King, U. Khan, K. Young, A. Gaucher, S. De, R. J. Smith, I. V. Shvets, S. K. Arora, G. Stanton, H. Y. Kim, K. Lee, G. T. Kim, G. S. Duesberg, T. Hallam, J. J. Boland, J. J. Wang, J. F. Donegan, J. C. Grunlan, G. Moriarty, A. Shmeliov, R. J. Nicholls, J. M. Perkins, E. M. Grieveson, K. Theuwissen, D. W. McComb, P. D. Nellist, V. Nicolosi, *Science* **2011**, *331*, 568.
- [6] a) E. Rokuta, Y. Hasegawa, K. Suzuki, Y. Gamou, C. Oshima, A. Nagashima, *Phys. Rev. Lett.* **1997**, *79*, 4609; b) W. Auwärter, M. Muntwiler, J. Osterwalder, T. Greber, *Surf. Sci.* **2003**, *545*, L735; c) A. B. Preobrajenski, A. S. Vinogradov, N. Mårtensson, *Surf. Sci.* **2005**, *582*, 21; d) J. Lu, P. S. Yeo, Y. Zheng, H. Xu, C. K. Gan, M. B. Sullivan, A. H. Castro Neto, K. P. Loh, *J. Am. Chem. Soc.* **2013**, *135*, 2368; e) K. K. Kim, A. Hsu, X. Jia, S. M. Kim, Y. Shi, M. Hofmann, D. Nezich, J. F. Rodriguez-Nieva, M. Dresselhaus, T. Palacios, J. Kong, *Nano Lett.* **2012**, *12*, 161; f) G. Kim, A. R. Jang, H. Y. Jeong, Z. Lee, D. J. Kang, H. S. Shin, *Nano Lett.* **2013**, *13*, 1834; g) Y. Shi, C. Hamsen, X. Jia, K. K. Kim, A. Reina, M. Hofmann, A. L. Hsu, K. Zhang, H. Li, Z. Y. Juang, M. S. Dresselhaus, L. J. Li, J. Kong, *Nano Lett.* **2010**, *10*, 4134; h) L. Song, L. Ci, H. Lu, P. B. Sorokin, C. Jin, J. Ni, A. G. Kvashnin, D. G. Kvashnin, J. Lou, B. I. Yakobson, P. M. Ajayan, *Nano Lett.* **2010**, *10*, 3209; i) A. Ismach, H. Chou, D. A. Ferrer, Y. Wu, S. McDonnell, H. C. Floresca, A. Covacevich, C. Pope, R. Piner, M. J. Kim, R. M. Wallace, L. Colombo, R. S. Ruoff, *ACS Nano* **2012**, *6*, 6378; j) K. K. Kim, A. Hsu, X. Jia, S. M. Kim, Y. Shi, M. Dresselhaus, T. Palacios, J. Kong, *ACS Nano* **2012**, *6*, 8583; k) Y.-H. Lee, K.-K. Liu, A.-Y. Lu, C.-Y. Wu, C.-T. Lin, W. Zhang, C.-Y. Su, C.-L. Hsu, T.-W. Lin, K.-H. Wei, Y. Shi, L.-J. Li, *RSC Adv.* **2012**, *2*, 111.
- [7] P. Sutter, J. Lahiri, P. Zahl, B. Wang, E. Sutter, *Nano Lett.* **2013**, *13*, 276.
- [8] S. Hagstrom, H. Lyon, G. Somorjai, *Phys. Rev. Lett.* **1965**, *15*, 491.
- [9] a) P. W. Sutter, J. I. Flege, E. A. Sutter, *Nat. Mater.* **2008**, *7*, 406; b) N. Liu, L. Fu, B. Dai, K. Yan, X. Liu, R. Zhao, Y. Zhang, Z. Liu, *Nano Lett.* **2011**, *11*, 297.
- [10] a) K. Yoshihara, M. Tosa, K. Nii, *J. Vac. Sci. Technol. A* **1985**, *3*, 1804; b) D. Fujita, T. Homma, *J. Vac. Sci. Technol. A* **1988**, *6*, 230; c) M. Xu, D. Fujita, H. Chen, N. Hanagata, *Nanoscale* **2011**, *3*, 2854.
- [11] S. Suzuki, R. M. Pallares, H. Hibino, *J. Phys. D: Appl. Phys.* **2012**, *45*, 385304.
- [12] Y. N. Dai, *Binary Alloy Phase Diagrams*, Science Press of China, Beijing, China **2009**.
- [13] L. Y. Jiao, B. Fan, X. J. Xian, Z. Y. Wu, J. Zhang, Z. F. Liu, *J. Am. Chem. Soc.* **2008**, *130*, 12612.
- [14] S. Reich, A. Ferrari, R. Arenal, A. Loiseau, I. Bello, J. Robertson, *Phys. Rev. B* **2005**, *71*, 205201.
- [15] L. Ci, L. Song, C. Jin, D. Jariwala, D. Wu, Y. Li, A. Srivastava, Z. F. Wang, K. Storr, L. Balicas, F. Liu, P. M. Ajayan, *Nat. Mater.* **2010**, *9*, 430.
- [16] R. V. Gorbachev, I. Riaz, R. R. Nair, R. Jalil, L. Britnell, B. D. Belle, E. W. Hill, K. S. Novoselov, K. Watanabe, T. Taniguchi, A. K. Geim, P. Blake, *Small* **2011**, *7*, 465.
- [17] H. Fang, H. A. Bechtel, E. Plis, M. C. Martin, S. Krishna, E. Yablonovitch, A. Javey, *Proc. Natl. Acad. Sci. USA* **2013**, *110*, 11688.
- [18] R. R. Nair, P. Blake, A. N. Grigorenko, K. S. Novoselov, T. J. Booth, T. Stauber, N. M. R. Peres, A. K. Geim, *Science* **2008**, *320*, 1308.
- [19] V. A. Margulis, E. E. Muryumin, E. A. Gaiduk, *Phys. B* **2012**, *407*, 4244.
- [20] M. Fox, *Optical Properties of Solids*, Oxford University Press, Oxford, UK **2001**.
- [21] L. Song, Z. Liu, A. L. M. Reddy, N. T. Narayanan, J. Taha-Tijerina, J. Peng, G. Gao, J. Lou, R. Vajtai, P. M. Ajayan, *Adv. Mater.* **2012**, *24*, 4878.
- [22] C. H. Zhang, L. Fu, N. Liu, M. H. Liu, Y. Y. Wang, Z. F. Liu, *Adv. Mater.* **2011**, *23*, 1020.